Proprioceptive State Estimation for Amphibious Tactile Sensing

Ning Guo[#], Xudong Han[#]
Department of Mechanical and Energy Engineering
Southern University of Science and Technology
Shenzhen, China 518055

Shuqiao Zhong[#], Zhiyuan Zhou, Jian Lin
Department of Ocean Science and Engineering
Southern University of Science and Technology
Shenzhen, China 518055

Jiansheng Dai
Institute of Robotics
Southern University of Science and Technology
Shenzhen, China 518055

Fang Wan[*]
School of Design
Southern University of Science and Technology
Shenzhen, China 518055
wanf@sustech.edu.cn

Chaoyang Song[*]
Department of Mechanical and Energy Engineering
Southern University of Science and Technology
Shenzhen, China 518055
songcy@ieee.org

December 18, 2023

Abstract

This paper presents a novel vision-based proprioception approach for a soft robotic finger capable of estimating and reconstructing tactile interactions in terrestrial and aquatic environments. The key to this system lies in the finger's unique metamaterial structure, which facilitates omni-directional passive adaptation during grasping, protecting delicate objects across diverse scenarios. A compact in-finger camera captures high-framerate images of the finger's deformation during contact, extracting crucial tactile data in real time. We present a method of the volumetric discretized model of the soft finger and use the geometry constraints captured by the camera to find the optimal estimation of the deformed shape. The approach is benchmarked with a motion-tracking system with sparse markers and a haptic device with dense measurements. Both results show state-of-the-art accuracies, with a median error of 1.96 mm for overall body deformation, corresponding to 2.1% of the finger's length. More importantly, the state estimation is robust in both on-land and underwater environments as we demonstrate its usage for underwater object shape sensing. This combination of passive adaptation and real-time tactile sensing paves the way for amphibious robotic grasping applications.

Keywords Soft Robotics · Tactile Sensing · State Estimation

1 Introduction

For robots to interact with the physical environment, the moment of touch holds the truth of dynamic interactions [1]. For most living organisms, the skin plays a crucial role in translating material properties, object physics, and interactive dynamics through sensory receptors into chemical signals processed by the brain [2] to formulate a *feeling* of the external environment (exteroception) [3] and the bodily self (proprioception) [4]. One stream of research focuses on

[*]Corresponding Authors.

developing novel tactile sensors [5], aiming at replicating the skin's basic functionality with comparable or superior performances [6]. Another stream of research considers robots while developing or utilizing tactile sensors [7], where integrating with robotic systems becomes a design challenge that requires an interdisciplinary approach [8], fostering a growing interest in tactile robotics among academia and industry [9].

1.1 Towards Dense Sensing for Tactile Robotics

Tactile sensory generally involves many properties that can be digitized for robotics [10]. For mechanics-based dynamics and control, the interactive force and torque on the contact surface are a primary concern in robotics [11], which could be generally approached as 1) Point-wise Sensing for 6D forces and torques (FT), 2) Bio-inspired Sparse Sensing Array and 3) Visuo-Tactile Dense Image Sensing, where a certain level of material softness or structural geometry are leveraged for an enhanced representation of the mechanic interactions into tactile data.

Point-wise Sensing for 6D FT: Estimating forces at contact points is paramount in robotic systems, enabling awareness of physical interaction between the robot and its surrounding objects [12]. Robotic research, especially when dynamics and mechanics are involved, is generally more interested in utilizing the force-and-torque properties for manipulation problems by robotic hands [13] or locomotion tasks by legged robots [14]. For a single reference point, the FT properties could be succinctly represented by a 6D vector of the forces along and the torques about the three orthogonal axes, making it comparable to the joint torque sensing in articulated robotic structures. However, the shortcut between physical contact and a point-wise 6D FT measurement may not capture the full extent of contact information for further algorithmic tasks [15].

Bio-inspired Sparse Sensing Array: Similar to the biological skin's super-resolutive mechanoreception for tactile sensing, a common approach in engineering is to place an array of sensing units on the interactive surface [16]. Instead of going for a localized 6D force and torque contact information, researchers usually tackle the problem with enhanced pressure sensing across its entire surface from spatially distributed sensing elements [17]. As a result, one can build models or implement learning algorithms to achieve super-resolution by sampling the discrete sensory inputs, producing a continuous estimation of the tactile interaction on the surface at a much higher resolution than the sensing array arrangement. Recent research [18] shows that one can leverage magnetic properties to achieve de-coupled normal and shear forces and simultaneously achieve super-resolutive tactile sensing of the normal and frictional forces for high-performing robotic grasping.

Visuo-Tactile Dense Image Sensing: Vision-based tactile sensing recently emerged as a popular approach to significantly increase the sensing resolution by leveraging the modern imaging process to visually track the deformation of a soft medium as the interface of physical interaction [19, 20, 21], eliminating the need for biologically inspired super-resolution [22]. Robotic vision has already become a primary sensing modality for advanced robots with the maturity of modern imaging technologies within a compact form factor [23] accessible to various software and algorithm libraries for real-time processing. While the high resolution of modern cameras offers significant advantages, the infinite number of potential configurations of the soft medium introduces a significant challenge [24].

1.2 Proprioceptive State Estimation

For tactile applications in robotics, proprioceptive perception of the joint position and movement of the body plays a critical role in achieving state estimation. The tactile interface is a physical separation between the intrinsic proprioception concerning the robot and the extrinsic perception concerning the object-centric environment. For the following, we focus on vision-based tactile sensing, which also applies to analyzing the other methods reviewed above.

Intrinsic Proprioception in Tactile Robotics: For vision-based intrinsic proprioception, the analysis is usually centered on estimating the state of the soft medium during contact, inferring tactile interaction [25]. To establish a physical correspondence between a finite parameterization state estimation model and an infinite configuration of soft deformation [26], markers that are easy to track are often used to discretize the displacement field of soft mediums. In [27], a simple blob detection method is introduced to track uniform distributed markers in a planar transparent soft layer for deformation approximation. Advanced image analysis [28] is also adopted to utilize machine learning algorithms to extract high-level deformation patterns from randomly spread markers over the entire three-dimensional volume of soft medium for robust state estimation [29]. Recent research [30] shows a promising approach to integrate physics-based models that capture the dynamic behavior of the soft medium under deformation.

Extrinsic Perception for Tactile Robotics: For extrinsic perception, the focus is shifted to estimating the object-level information, including object localization, shape and dynamics parameters, etc. [31], where tactile sensing data could be used for task-based manipulation and locomotion. Using contact to estimate an object's global geometry is instrumental for intelligent agents to make better decisions during object manipulation [32]. Usually, tactile sensing is employed for

estimating the object's shape in visually occluded regions, thus playing a complementary role to vision sensors [33, 34]. However, in scenarios where a structured environment with reliable external cameras is unavailable or impractical, such as during exploration tasks in unstructured environments, tactile sensing can provide valuable feedback to achieve environmental awareness [35].

1.3 Amphibious Tactile Robotics

Amphibious environments present a unique and dynamic challenge for robotic systems. Robots operating in these environments must contend with vastly different physical properties, including changes in buoyancy, friction, and fluid dynamics [36]. Furthermore, the transition between water and air requires robots to adapt their sensory systems and control strategies to function effectively in each medium [37].

Developing effective tactile sensors for amphibious robots presents several challenges. Sensors must be robust enough to withstand the harsh aquatic environment and be sensitive enough to detect subtle changes in water and air [38]. The transition between these two media can also cause sensor drift and require calibration to maintain accuracy [39]. Despite these challenges, there are exciting opportunities in amphibious tactile robotics, with improved sensitivity, durability, and resistance to environmental factors [40]. However, a research gap remains in developing an effective tactile sensing method with an integrated design on the finger surface or fingertip that directly applies to amphibious applications.

1.4 Proposed Method and Contributions

This paper introduces a novel vision-based proprioception approach for a soft robotic finger, enabling the estimation and reconstruction of tactile interactions in terrestrial and aquatic environments. This is achieved by leveraging the finger's metamaterial structure, which allows for omni-directional passive adaptation, protecting delicate objects during grasping across diverse scenarios. The proposed system employs a compact in-finger camera to capture high-framerate images of the soft finger's morphology during contact, extracting crucial tactile data. The metamaterial structure of the finger allows for omni-directional passive adaptation, safeguarding fragile objects during grasping in both water and air. The in-finger camera enables real-time extraction of tactile data from the finger's deformation, providing valuable insights into the physical interaction. This combination of passive adaptation and real-time tactile sensing makes the proposed system well-suited for amphibious robotic grasping applications. Here are the contributions of this study:

- Proposed and validated a model-based synthesis of morphological deformation for an omni-adaptive soft robotic finger using in-finger vision.
- Formalized a contact-based object surface estimation approach using a spatial discretized elastic model.
- Evaluated the proprioceptive state estimation performance of the soft omni-adaptive finger with demonstrated performance for underwater object shape estimation.

This paper is organized as follows. Section 2 provides the design of an omni-adaptive soft finger. Section 3 presents a proprioceptive shape modeling and estimation method. Section 4 addresses touch sensing for contact object shape estimation. Experiment results are shown in Section 5. In Section 6 we discuss sensorization and morphological design of the soft finger for touch sensing. Section 7 includes conclusion, limitations, and future works.

2 Omni-adaptive Metamaterial Design with In-Finger Vision

Soft grippers can achieve diverse and robust grasping behaviors with a relatively simple control strategy [41]. This study adopts a vision-based approach to enable tactile perception for a soft robotic finger, as shown in Fig. 1A. The finger geometry features a shrinking cross-sectional network towards the tip based on our previous work [42, 43], fixed on a transparent support frame by a mounting plate. A rigid plate pasted with an ArUco tag is mechanically fixed with the four lower crossbeams of the soft finger. To capture the pose of the tag, a monocular RGB camera with a field of view (FOV) of $130°$ is installed inside the support frame facing towards the cavity of the finger, which is capable of video recording at a high frame rate at 120 FPS (frames per second) and a resolution of 640×480 pixels. During the interaction between the finger and the external environment, the real-time image captured by the camera provides the pose data of the ArUco tag as rigid-soft kinematics coupling constraints for the proprioceptive state estimation of the finger.

The finger is fabricated by vacuum molding using Hei-cast 8400, a three-component polyurethane elastomer. Based on the previous experience [44], we mixed the three components with a ratio of 1:1:0, producing a hardness of 90 (Type A) to achieve reliable bending and enveloping capabilities. The proposed soft finger exhibits complex adaptive
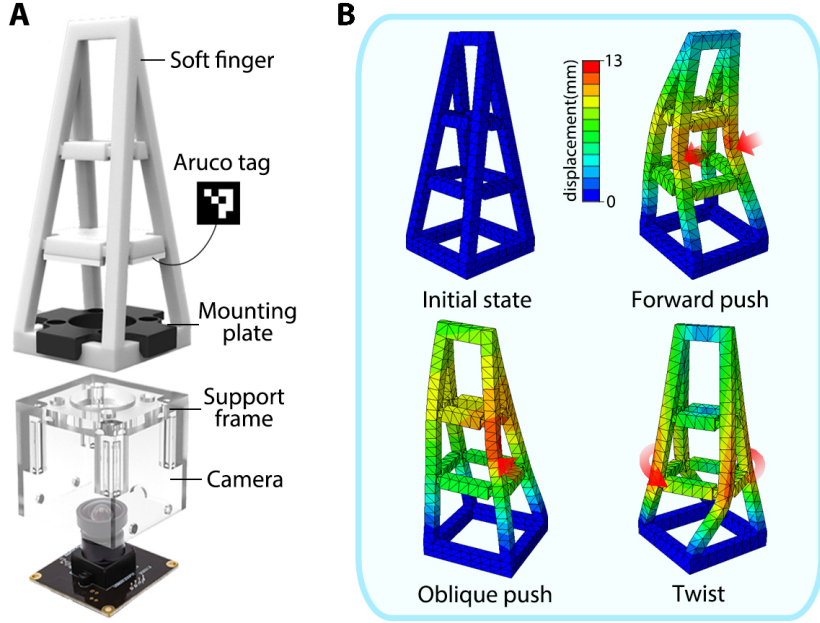
Figure 1: **Assembly and omni-adaptive capability of the soft finger.** (A) The assembly consists of a soft finger, a rigid plate pasted with an ArUco tag, a mounting plate, a support frame, and a camera. (B) The finger deformation by forward push, oblique push, and twist shows the omni-adaptive capability.

deformations, such as forward push, oblique push, and twist, as shown in Fig. 1B. Due to the capability of omni-directional adaptation on the finger surface to unknown object geometries, it enables a passive form-closure for robotic grasping [45].

3 Shape Deformation Modelling and Estimation

For the volumetric soft finger, we consider a 3D space $\mathbf{\Omega} \in \mathbb{R}^3$ filled with homogeneous elastic material. Under different boundary conditions, the distribution of internal elastic energy within the soft body varies significantly. The objective of proposed proprioceptive state estimation methodology is to accurately determine the smooth deformation map, $\Phi : \mathbf{\Omega} \to \tilde{\mathbf{\Omega}}$, that facilitates the geometric transformation of the soft body from its initial configuration, represented by $\mathbf{\Omega}$, to a deformed configuration, denoted as $\tilde{\mathbf{\Omega}}$. This transformation is characterized by minimizing a form of variational energy measuring the distortion of the soft body [46]. As a result, the proposed computational approach to soft finger shape reconstruction highly depends on finite element discretization and the choice of energy function that characterizes deformation.

3.1 Volumetric Parameterization of Deformation

Denote the tetrahedral mesh of discretized soft body by $\mathcal{M} = \{\mathcal{V}, \mathcal{T}\}$ where $\mathcal{V} = \{\mathbf{x}_1, ..., \mathbf{x}_n\}$ is the set of vertices $\mathbf{x}_i \in \mathbb{R}^3$, and $\mathcal{T} = \{t_1, ..., t_m\}$ is the set of tetrahedra elements, as shown in Fig. 2A(i).

When the soft body deforms, a collection of chosen linear approximated local deformation maps are applied to $\mathcal{M}$, over each tetrahedron element t_j via an affine transformation:

$$\Phi|_{t_j}(\mathbf{X}) = \mathbf{A}_{t_j}\mathbf{X} + \mathbf{b}_{t_j}, \tag{1}$$

where $\mathbf{X} \in \mathbb{R}^3$ stands for all points inside element t_j, $\mathbf{A}_{t_j} \in \mathbb{R}^{3 \times 3}$ is the differential part of the deformation map and $\mathbf{b}_{t_j} \in \mathbb{R}^3$ is the translation part. We choose this piecewise linear deformation map over each tetrahedron for computational efficiency. Besides, high-order deformation functions can be used for better approximation [47].

As shown in Fig. 2A(ii), for any t_j element, the local affine transformation applied on each vertex is denoted as:

$$\begin{bmatrix} \mathbf{A}_{t_j} & \mathbf{b}_{t_j} \end{bmatrix} \cdot \begin{bmatrix} \mathbf{X}_{t_j}^1 & \mathbf{X}_{t_j}^2 & \mathbf{X}_{t_j}^3 & \mathbf{X}_{t_j}^4 \\ \mathbf{1} & \mathbf{1} & \mathbf{1} & \mathbf{1} \end{bmatrix} = \begin{bmatrix} \mathbf{x}_{t_j}^1 & \mathbf{x}_{t_j}^2 & \mathbf{x}_{t_j}^3 & \mathbf{x}_{t_j}^4 \end{bmatrix}, \tag{2}$$

where $\mathbf{x}_{t_j}^i \in \mathbb{R}^3$, $i \in \{1, 2, 3, 4\}$, are the deformed vertices location of t_j tetrahedron, $\mathbf{X}_{t_j}^i \in \mathbb{R}^3$ are corresponding initial vertices location.

Given the locations of initial vertices, the deformation gradient $\mathbf{A}_{t_j}$ in the chosen piecewise linear transformation Eq. 1 can be expressed as a linear combination of unknown deformed element vertices location $\mathbf{x}_{t_j}$ as :

$$\mathbf{A}_{t_j}(\mathbf{x}_{t_j}) = \frac{\partial\Phi|_{t_j}}{\partial\mathbf{X}} = \mathbf{D}_s(\mathbf{x}_{t_j}) \cdot \mathbf{D}_m^{-1}(\mathbf{X}_{t_j}), \tag{3}$$

where

$$\mathbf{D}_s(\mathbf{x}_{t_j}) = \begin{bmatrix} \mathbf{x}_{t_j}^2 - \mathbf{x}_{t_j}^1 & \mathbf{x}_{t_j}^3 - \mathbf{x}_{t_j}^1 & \mathbf{x}_{t_j}^4 - \mathbf{x}_{t_j}^1 \end{bmatrix}, \tag{4}$$

$$\mathbf{D}_m(\mathbf{X}_{t_j}) = \begin{bmatrix} \mathbf{X}_{t_j}^2 - \mathbf{X}_{t_j}^1 & \mathbf{X}_{t_j}^3 - \mathbf{X}_{t_j}^1 & \mathbf{X}_{t_j}^4 - \mathbf{X}_{t_j}^1 \end{bmatrix}. \tag{5}$$

For the discretized tetrahedral mesh $\mathcal{M}$, the collection of deformation maps $\{\Phi_{t_j}\}_{t_j \in \mathcal{T}}$ for all tetrahedra elements should uniquely determine the deformed shape of the soft body [48].

3.2 Geometry-Related Deformation Energy Function

To mimic the physical deformation behavior, the specific energy function form of the deformation map $\Psi(\Phi_{t_j})$ needs to be prescribed. Several proper forms of geometry-related deformation energies have been proposed, such as as-rigid-as-possible [49], conformal distortion [50], and isometric distortion [51].

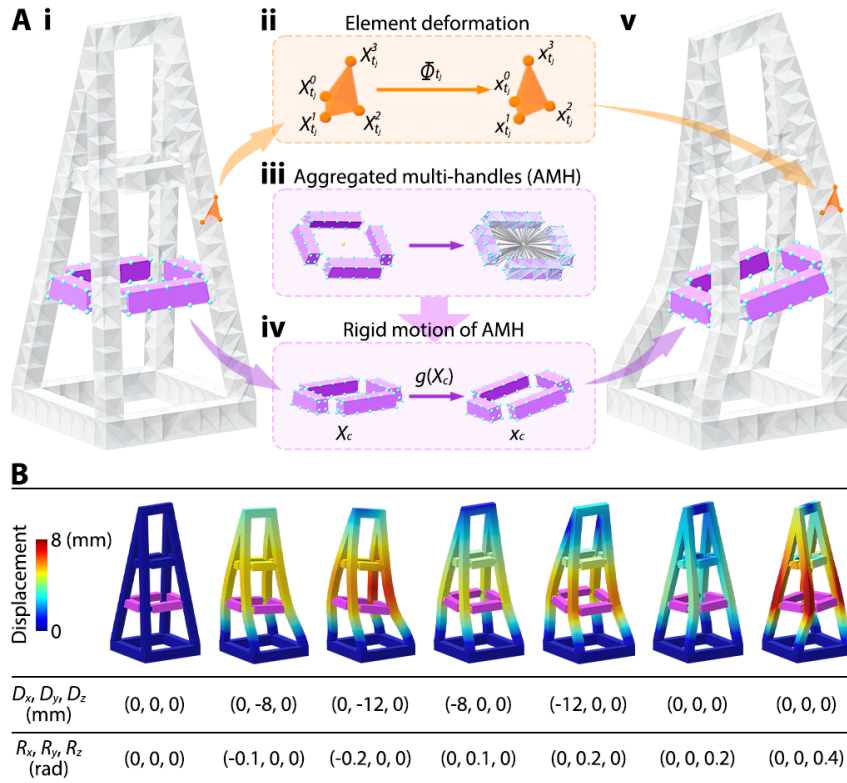| D_x, D_y, D_z (mm)	(0, 0, 0)	(0, -8, 0)	(0, -12, 0)	(-8, 0, 0)	(-12, 0, 0)	(0, 0, 0)	(0, 0, 0)
R_x, R_y, R_z (rad)	(0, 0, 0)	(-0.1, 0, 0)	(-0.2, 0, 0)	(0, 0.1, 0)	(0, 0.2, 0)	(0, 0, 0.2)	(0, 0, 0.4)

Figure 2: **Proprioceptive deformation modeling and estimation of Omni-Adaptive Soft Finger.** (A) Representation of the proprioceptive model, including i) Initial undeformed configuration Ω of the soft finger, discretized using tetrahedral mesh; ii) Local affine mapping Φ_{t_j} applies on t_j element, transforming each vertex from $\mathbf{X}_{t_j}^i \in \mathbb{R}^3$ to $\mathbf{x}_{t_j}^i \in \mathbb{R}^3$, $i \in \{1, 2, 3, 4\}$; iii) Approximation of visual observed marker area as Aggregated Multi-Handles (AMH) on the tetrahedral mesh (xx colored); iv) Applies uniform rigid motion $g \in SE(3)$ on all AMH that drives soft finger to a deformed configuration $\tilde{\Omega}$. (B) Demonstration of soft finger deformation reconstructions under a series of rigid motions applied on AMH, including bending and twisting.

Instead of deriving the energy of the system explicitly using constitutive relation and balance equations [52], we directly choose a symmetric Dirichlet form of energy function to characterize the deformation [53], which indicates isometric distortion and behaves well in the case of our soft finger. As the deformation should be irrelevant to the translation, the discrete element energy functional only takes augment of the gradient of each deformation maps $\{\Phi_{t_j}\}_{t_j \in \mathcal{T}}$ as:

$$\Psi(\Phi_{t_j}) = \Psi(\mathbf{A}_{t_j}) = ||\mathbf{A}_{t_j}||_{\mathcal{F}}^2 + ||\mathbf{A}_{t_j}^{-1}||_{\mathcal{F}}^2, \tag{6}$$

where $|| \cdot ||_{\mathcal{F}}$ is the Frobenius norm. The accumulated discrete element energy functional of the soft body denotes:

$$E(\mathbf{x}) = \sum_{t_j \in \mathcal{T}} \Psi(\mathbf{A}_{t_j}(\mathbf{x})), \tag{7}$$

where $\mathbf{x} \in \mathbb{R}^{3 \times n}$ contains all the discretized vertices location of the soft body $\mathcal{M}$.

3.3 Rigidity-Aware Aggregated Multi-handles Constraints from Visual Observation

Compared to multi-view systems, the wide availability and ease of use make monocular cameras one of the best choices to achieve environmental perception. However, deformable shape reconstruction from 2D image observations is well-known as an ill-posed inverse problem and has been actively researched [54]. To make this problem trackable, we leverage the volumetric discretized model described above and introduce rigidity-aware aggregated multi-handle constraints to reliably reconstruct the soft finger's deformed shape.

As shown in Figs. 2A(iii)&(iv), a rigid plate is mechanically coupled with part of soft material, resulting in a uniform rigid transformation g for each attached node in the discrete model M.

$$\mathbf{x}_h = g(\mathbf{X}_h), \tag{8}$$

where $\mathbf{x}_h \in \mathbb{R}^{3 \times p}$ contains deformed location of p vertices related to the rigidity-aware aggregated multi-handles constraints, while $\mathbf{X}_h \in \mathbb{R}^{3 \times p}$ contains the corresponded undeformed vertices location. The rigid transformation g is estimated using fiducial markers, widely used in robot vision tasks.

3.4 Shape Estimation by Geometric Optimization

With the discrete energy functional Eq. 7 of the given soft body $\mathcal{M}$ and observed kinematics constraints Eq. 8, soft body shape estimation can be directly translated into a constrained geometry optimization problem as:

$$\min_{\mathbf{x}} \quad \sum_{t_j \in \mathcal{T}} \Psi(\mathbf{A}_{t_j}(\mathbf{x})),$$
$$\text{s.t.} \quad \mathbf{x}_h = g(\mathbf{X}_h). \tag{9}$$

Instead of considering kinematics constraints as hard boundary conditions, we enforce them by appending quadratic penalty functions to original functional $E(\mathbf{x})$ in Eq. 7 for easier handling, which results in

$$\tilde{E}(\mathbf{x}) = \sum_{t_j \in \mathcal{T}} \Psi(\mathbf{A}_{t_j}(\mathbf{x})) + \omega||\mathbf{x}_h - g(\mathbf{X}_h)||^2, \tag{10}$$

and the deformed shape can be estimated by minimizing the augmented energy functional in Eq. 10 as:

$$\mathbf{x}^* = \arg\min_{\mathbf{x}} \tilde{E}(\mathbf{x}; \omega, g), \tag{11}$$

where ω is the penalty parameter for the corresponding unconstrained minimization problem. Note that a more considerable penalty weight will lead to better constraint satisfaction but poor numerical conditions.

In practice, we set $\omega = 10^5$ and compute the deformed vertices positions $\mathcal{V}$ by iteratively minimizing Eq. 11 using a Newton-type solver as shown in Alg. 1. As shown in Fig. 2B, a series of physically plausible deformations of the soft finger under observed constraints are reconstructed in real-time using the proposed optimization approach.

4 Object Shape Estimation using Tactile Sensing

While proprioception refers to being aware of one's movement, tactile sensing involves gathering information about the external environment through the sense of touch. This section presents an object shape estimation approach by extending the proprioceptive state estimation method proposed in Section 3 to tactile sensing.

Since passive adaptive structures can quickly adapt their shape to conform to contact objects, we could infer shape-related contact information from the estimated shape of the soft finger during contact. By assuming that the contact patch on the soft finger coincides with that of the object during grasping, we can predict object surface topography using spatially distributed contact points on the contact interface.

6

Algorithm 1 Projected Hessian Algorithm

1: **Input**: Rigid transformation of AMH g
2: **Output**: Estimated positions of deformed vertices $\mathbf{x}^*$
Require:
    Vertices positions of current shape $\mathbf{x}_0$
    Convergence tolerance ϵ
    Maximum number of iterations $N_{\max}$
3: $k \leftarrow 0$
4: Compute gradient $d_k = \nabla \tilde{E}(\mathbf{x}_k)$
5: And Hessian $H_k = \nabla^2 \tilde{E}(\mathbf{x}_k)$
6: **while** $\|d_k\| > \epsilon$ and $k < N_{\max}$ **do**
7:     Solve $H_k \Delta \mathbf{x}_k = -d_k$ for $\Delta \mathbf{x}_k$
8:     Project $\Delta \mathbf{x}_k$ onto the feasible region
9:     Update iterate: $\mathbf{x}_{k+1} \leftarrow \mathbf{x}_k + \Delta \mathbf{x}_k$
10:     $k \leftarrow k + 1$
11: **end while**
12: iteration stop $\mathbf{x}^* = \mathbf{x}_k$

4.1 Contact Interface Points Extraction

Based on the spatial discretization model in Section 3.1, an indexed set $\mathcal{I} = \{c_1, c_2, ..., c_k\}$ of nodes located at upper area of the soft finger mesh $\mathcal{M}$ are extracted as contact interface points, as shown in Fig. 3A.

Each time with the observed AMH constraints input, we could determine the positions of these contact interface points by first solving Eq. 11, then extracting corresponding nodes using indexed set $\mathcal{I}$, from solved deformed positions of vertices $\mathcal{V}$: $\mathbf{x}_c = \{\mathbf{x}_i | \mathbf{x}_i \in \mathcal{V}, i \in \mathcal{I}\}$.

4.2 Implict Surface Representation for Object Shape

Considering the grasping action using a soft finger as a multi-point tactile probing, the object surface patches could be progressively reconstructed by these gripping actions with collected positions of contact interface points $\mathbf{x}_c$ extracted from the soft finger.

An implicit surface representation is defined by a function that can be evaluated at any point in space, which yields a value indicating whether the point is inside the object, outside the object, or on the object's surface. For the 3-D space
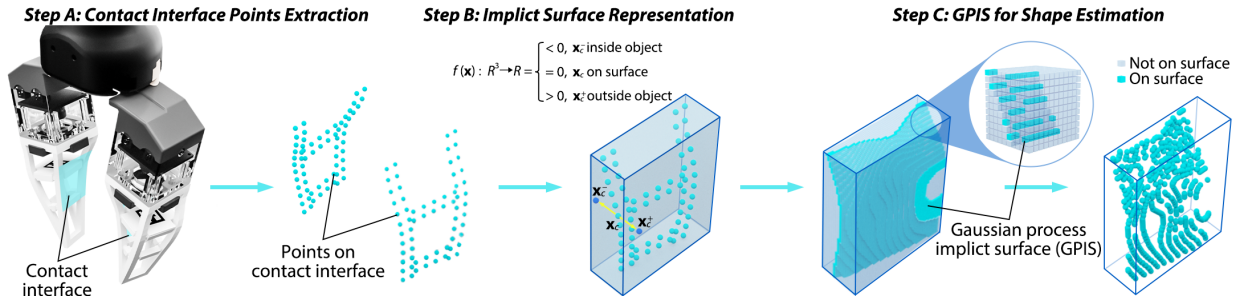

Figure 3: **Pipeline for contact interface geometry sensing using deformed positions of soft finger mesh nodes.** (A) Owing to the ability of the soft finger to deform and adapt its shape to fit the contours of the object being grasped, we take the deformed soft finger mesh nodes as approximate multi-contact points on the contact interface. (B) In addition to the mesh nodes $\mathbf{x}_c$ on the contact interface, auxiliary training points $\mathbf{x}_c^-$ and $\mathbf{x}_c^+$ are generated in this step to increase the accuracy of the implicit surface reconstruction. (C) Gaussian process implicit surface model is adopted for contact object surface patch estimation.

considered in our problem, this function f is defined as:

$$f(\mathbf{x}) : \mathbb{R}^3 \to \mathbb{R} = \begin{cases} < 0, & \text{if } \mathbf{x} \text{ inside the object;} \\ = 0, & \text{if } \mathbf{x} \text{ on the surface;} \\ > 0, & \text{if } \mathbf{x} \text{ outside the object.} \end{cases} \tag{12}$$

As is shown in Fig. 3B, we only collected positions of partial contact interface points $\mathbf{x}_c$, which are assumed to coincide with the object surface for each gripping action. While surface points are observed, we do not explicitly observe off-surface or internal points exemplars. For those unobserved cases in Eq. 12, we generate control points of the corresponding two types to express the directional information of the surface using the method described in [55].

4.3 GPIS for Surface Estimation

An object's shape is estimated by finding the points with zero value of implicit surface function Eq. 12 (i.e., the isosurface) in a 3D region of interest. Gaussian process implicit surface (GPIS), as a non-parametric probabilistic method [56], is a powerful tool for object surface reconstruction from partial or noisy 3D data and often used in the context of tactile and haptic exploration [57, 58].

A Gaussian Process (GP) is a collection of N random variables with a joint Gaussian distribution and, therefore, can be completely specified by its mean and covariance functions. Given the collected contact interface points togeter with generated control points positions $\mathcal{X} = \{\mathbf{x}_1, \mathbf{x}_2, ..., \mathbf{x}_N\}$ for each gripping action and corresponding observed values $\mathcal{Y} = \{\mathbf{y}_1, \mathbf{y}_2, ..., \mathbf{y}_N\}$, such that $\mathbf{y}_i = f(\mathbf{x}_i) + \epsilon$, where $\epsilon \sim \mathcal{N}(0, \sigma_\epsilon^2)$ denotes Gaussian noise with zero mean and σ_ϵ^2 variance, the GP can be written as $f(\mathbf{x}) \sim \mathcal{GP}(m(\mathbf{x}), k(\mathbf{x}, \mathbf{x}'))$, where, $m(\mathbf{x})$ is the mean function and $k(\mathbf{x}, \mathbf{x}')$ is the covariance function [59]. In our implementation, we use the radial basis function kernel, which is characterized by the two hyper-parameters the variance σ_f^2 and the length scale l:

$$k(\mathbf{x}, \mathbf{x}') = \sigma_f^2 \exp\left(-\frac{||\mathbf{x} - \mathbf{x}'||^2}{2l^2}\right). \tag{13}$$

With the covariance function and the observation data, the predictive mean $\bar{f}(\mathbf{x}^*)$ and variance $\bar{\mathcal{V}}(\mathbf{x}^*)$ at a query point $\mathbf{x}^*$ are:

$$\bar{f}(\mathbf{x}^*) = \mathbb{E}[f(\mathbf{x}^*)|\mathcal{X}, \mathcal{Y}, \mathbf{x}^*] = k(\mathcal{X}, \mathbf{x}^*)^\mathrm{T} \Sigma \mathcal{Y}, \tag{14}$$

$$\bar{\mathcal{V}}(\mathbf{x}^*) = k(\mathbf{x}^*, \mathbf{x}^*) - k(\mathbf{x}^*, \mathbf{x})^\mathrm{T} \Sigma k(\mathbf{x}^*, \mathbf{x}), \tag{15}$$

where $\Sigma = (k(\mathcal{X}, \mathcal{X}) + \sigma_\epsilon^2 \mathcal{I})^{-1}$. After voxelizing the bounding box volume enclosing the partially deformed finger-object interface, the zero-mean isosurface can be extracted from posterior estimation, which approximates the local shape of a grasped object, as is shown in Fig. 3C.

5 Experimental Results

We implemented our geometric optimization-based shape estimation algorithm (Alg. 1) for the soft finger in C++ and tested it on a standard PC with an Intel Core™ i7 3.8GHz CPU and 16 GB RAM. With the help of algorithmic differentiation of the numerical solver, Eigen [60], our system can realize the computation of the soft finger shape deformation with 3k tetrahedra in real-time (up to 20 fps).

This section presents the results of proprioceptive shape estimation of the soft finger using two experiment setups. One experiment leverages motion capture markers as ground truth, which provides high-precision but sparse measurements. The other experiment uses a Touch haptic device for ground truth data collection, which is less accurate but contains larger measuring coverage on the soft finger.

5.1 Comparisons with the Conventional Method

This section presents the performance of our shape estimation method by comparing it with two conventional methods, ABAQUS and as-rigid-as-possible (ARAP) [61]. Table 1 compares run time and mean error of shape estimation. Five different meshes with different numbers of elements, including 1k, 1.5k, 3k, 6k, and 12k, were provided, and the three methods were tested on the meshes with six different kinds of motions applied on AMH shown in Fig. 2B. It can be observed that our method can be 40 times faster than ABAQUS and two times faster than ARAP. We also compared the mean errors of all nodes estimated by our method and ARAP when benchmarked against ABAQUS. The results show that our method's mean error becomes more minor, from 0.346 mm to 0.086 mm, as the number of elements becomes

Table 1: RUN TIME AND MEAN ERROR COMPARISONS OF ABAQUS, ARAP, AND OUR METHOD

Number of Elements		1k	1.5k	3k	6k	12k
	ABAQUS	16.7	17.1	18.7	22.1	27.8
Run Time (s)	ARAP	0.0485	0.0776	0.151	0.304	0.703
	Ours	0.0231	0.0452	0.0905	0.241	0.639
	ABAQUS	NA	NA	NA	NA	NA
Mean Error* (mm)	ARAP	0.857	0.902	0.754	0.878	0.926
	Ours	0.346	0.149	0.130	0.143	0.086

*: The benchmark of mean error is ABAQUS.

more extensive, while ARAP's error remains 0.7-1.0 mm for different meshes. We also observe that the error of our method significantly decreases from 1k to 1.5k mesh while the error reduction from 1.5k to 12k is minimal. In terms of both running time and error, our approach has a significant advantage over ABAQUS and ARAP. In addition, 1.5k mesh is the most appropriate for our method, with both faster run speed and smaller error, which was selected for real-time estimation in the following experiments.
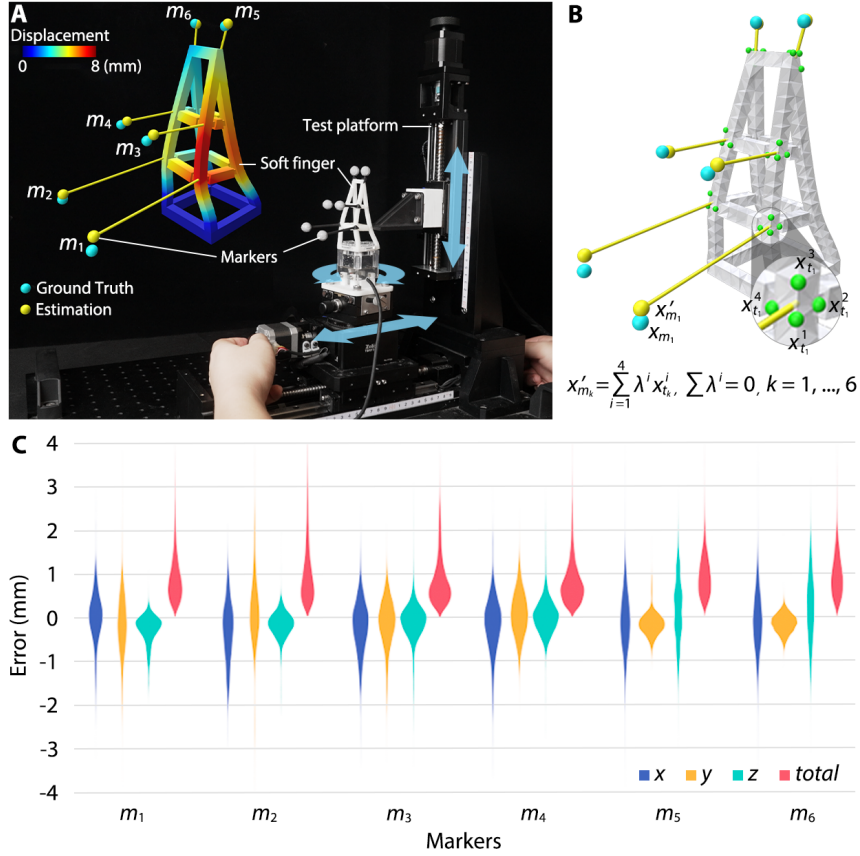

Figure 4: **Estimated marker deformation obtained by proposed proprioceptive shape estimation method.** (A) Experimental setup, including the soft finger, embedded with an RGB camera, a manual three-axis motion test platform, and six motion capture markers $m_1, m_2, ..., m_6$, rigidly attached to the soft finger. (B) The estimated position of the marker x'_{m_k} is calculated using the barycentric coordinate of the corresponding attached tetrahedron t_k, while the ground truth reading x_{m_k} is obtained from the motion capture system. (C) The corresponding error for each marker's three-dimensional deformation and total norm.

5.2 Deformation Estimation with Motion Capture Markers

As is shown in Fig. 4A, the soft finger is mounted on a three-axis motion platform to perform a set of deformed configurations for shape estimation. The test platform is operated manually to generate a set of different contact configurations between the soft finger and the indenter. During the process, the embedded camera streams real-time image data at a resolution of 640×480 pixels. The detected AMH rigid motion, using an off-the-shelf ArUco detection library [62], is fed into our implemented program for shape estimation.

Nokov vision system with client software tool tracks finger deformation and motion. A total of six motion capture markers with an 8 mm radius were used in the experiment. Markers are divided into three pairs and are rigidly attached to the fingertip (m_5, m_6), the first layer (m_3, m_4), and the second layer of the soft finger (m_1, m_2), respectively. Besides the markers used for soft finger deformation tracking, three other markers are attached to the platform and used as the reference reading to align the motion capture system's reference frame with the deformation computation coordinate frame.

The markers are attached to the soft finger with rigid links. To avoid occlusion while tracking markers, we design the connecting links in three types of lengths, as shown in Fig. 4B. We assume that each marker is rigidly attached to the nearest tetrahedron on the parameterized mesh model $\mathcal{M}$ and represent the location of the estimated marker using barycentric coordinates of the corresponding tetrahedron element in the deformed configuration of the soft finger:

$$\mathbf{x}'_{m_k} = \sum_{i=1}^{4} \boldsymbol{\lambda}^i_{t_k} \cdot \mathbf{x}^i_{t_k}, k \in \{1, 2, ..., 6\}, \tag{16}$$

$$\sum_{i=1}^{4} \boldsymbol{\lambda}^i_{t_k} = 0, t_k \in \mathcal{T}. \tag{17}$$

Due to the rigid connection assumption, the barycentric coordinates $\boldsymbol{\lambda}_{t_k}$ are constant during the deformation. After solving barycentric coordinates in Eq. 16 using the initial undeformed vertex position of the tetrahedron and corresponding tracked marker position without contact, the marker position prediction model is a linear combination of deformed vertex position of the corresponding tetrahedron resulting from geometric optimization Alg. 1 using calibrated barycentric coefficients. See Movie S1 in the Supplementary Materials for a video demonstration.

We visualize the error distribution with 3k data pairs of six markers' estimated and ground truth positions as illustrated in Fig. 4C. The norm of the total error of all experiment records for six markers is around $(0, 3)$ mm, while error distribution along each axis is centered around the $(-2, 2)$ mm range. As the marker prediction model in Eq. 16 comprises calibration and geometric optimization, the error distribution of six sparse markers may not be enough to validate the proposed method, leading to another dense measurement experiment in the following section.

5.3 Deformation Estimation using Touch Haptic Device

To further evaluate the proprioceptive shape estimation method using dense measurements, we designed another validation experiment with the position of pen-nib of a touch haptic device as ground truth measurement.

As is shown in Fig. 5A, the pen-nib of a Touch haptic device is used to stick tightly to some contact point on the soft finger and push forward five times during the experiment. We randomly sample fifty contact points covering half of the soft finger's sides and record the pen-nib's position and the corresponding point on the estimated deformed mesh model.

Similar to the calibration process of the experiment using a motion capture system, we solve the barycentric coordinates in Eq. 16, using the initial sticking position of pen-nib and the undeformed vertex position of the tetrahedron nearest to the sticking point. Since there is no slipping between the contact point and the pen-nib, recording the pushing position of the pen-nib for a randomly selected point is equivalent to collecting the ground truth deformation field of the soft finger evaluated at that point. Three pushing path points and the corresponding error between estimation and ground truth for three randomly selected contact locations are demonstrated in Fig. 5B. The pushing duration lasts ten seconds for each selected contact location, and the data is recorded at a sampling frequency of 20 Hz. Due to the variation among the pushing path for three contact locations, the error distribution exhibits slightly different, but all lie in the $(0, 2.5)$ mm range.

Compared with the experiment using six motion capture markers for shape estimation evaluation, the measurement points using the Touch device are dense and have more extensive coverage of the soft finger, revealing the spatial error distribution of the estimation method. As is shown in Fig. 5C, mean errors of deformation estimation evaluated at fifty randomly selected contact locations are visualized. Two side views of continuous error distribution for the soft finger are interpolated with errors of fifty sampled locations using a Gaussian-kernel-based nearest neighbor method [63].
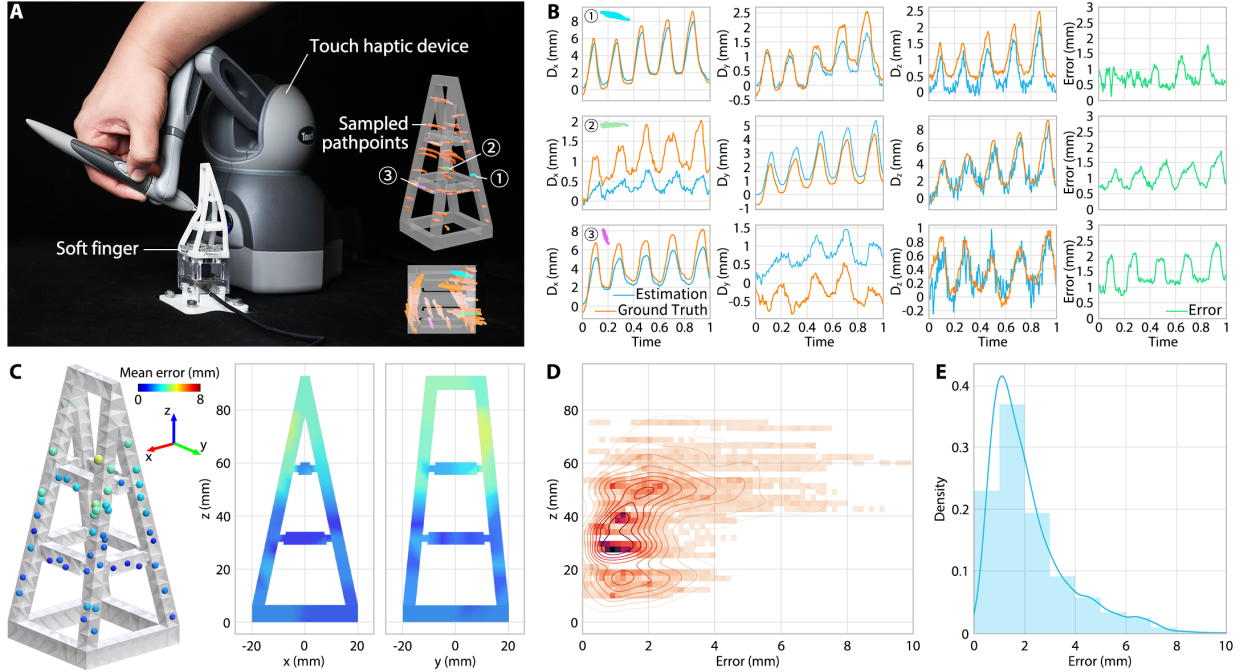
Figure 5: **Estimated deformation field of the soft finger using the proprioceptive shape estimation method.** (A) The Touch haptic device is used to make contact with the soft finger at different locations, while at the same time, the ground-truth positions and the reconstructed positions of contact points are recorded. (B) The pushing path points for three-dimensional and corresponding error of three distinct contact locations during the experiment. (C) The pen-nib of the touch haptic device is commanded to be pushed forward five times at fifty locations on the half sides of the soft finger. The map of the mean error norm is interpolated using fifty sampled contact locations. (D) The distribution of corresponding total error norm along the Z axis of the soft finger. (E) The corresponding total error norm of sampled contact points.

The error at contact locations near the observed AMH constraint should be smaller since violation of the AMH constraint will be penalized during the deformation shape optimization. We plot the error distribution of fifty sampled locations along the Z axis, as shown in Fig. 5D. The error at the contact location with a similar height to the AMH constraint is less and more concentrated. The error histogram of overall experiment records is shown in Fig. 5E, where the median of estimated error for whole body deformation is 1.96 mm, corresponding to 2.1% of the finger's length. See Movie S2 in the Supplementary Materials for a video demonstration.

5.4 Underwater Exteroceptive Estimation of Object Shape

As is shown in Fig. 6A, we mounted the integrated soft finger on the Robotiq's Hand-E gripper and attached the whole design at the end of a Franka Emika Panda robotic manipulator with an extension link. The gripper has an ingress protection rating of IP67, and we verified its consistent performance for temporary submergence under the water between 0.15 m and 1 m for 30 minutes. Our previous work extensively tested the gripper's underwater servoing capabilities for reactive grasping [64]. In this study, we use the same gripper for underwater object shape estimation in a lab tank. For more intensive usage underwater in the field, one can always replace the Hand-E gripper with a more appropriate one.

With the gripper submerged underwater, the grasping system is programmed to sequentially execute a series of actions, including gripping the object, releasing the object, and moving along a prescribed direction for a fixed distance for underwater object shape information acquisition. See Movie S3 in the Supplementary Materials for a video demonstration.

The experiment setup is shown in Fig. 6B(i). By mounting the target object at the bottom of the tank, we assume:

- The object's pose is fixed and calibrated with the gripper.
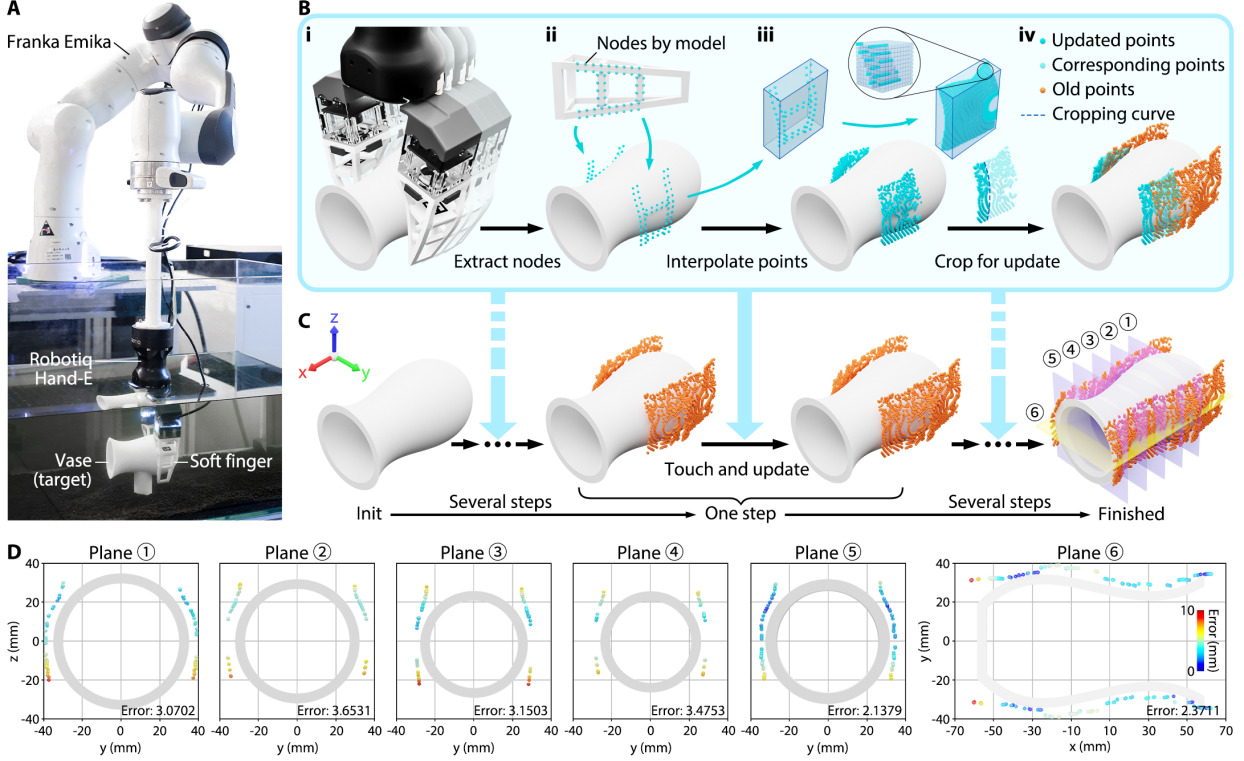- Passive object shape exploration is considered for object coverage.

Figure 6: **Underwater shape estimation of a vase using proprioceptive state estimation of the soft finger.** (A) Experimental setup for underwater shape estimation, where a Robotiq Hand-E gripper, installed with two proprioceptive soft fingers and an extension link, is mounted on a Franka Emika Panda robot arm. The gripper is programmed to perform a series of actions periodically, including gripping, releasing, and moving along the x-axis for a fixed distance. At the same time, a vase is fixed at the bottom of the tank in the lab. (B) Contact surface patch prediction using Gaussian process implicit surface (GPIS) with the soft finger. (C) Experiment pipeline for underwater shape estimation of a vase. (D) Evaluation of the reconstructed vase shape on some cutting sectional planes, measured in Chamfer Distance.

The inference of the GPIS model is computationally intractable for the large N measurement that accrues from high-dimensional tactile measurements. Instead of predicting the whole object surface by accumulating all the collected data, we only query a local GPIS model approximated using current observed contact data in a local focus area and build the surface incrementally.

Local GPIS Model Inference: A training set containing contact interface points $\mathbf{x}_c$ and corresponding augmented control points are collected each time a grasping action is performed. Before querying the local GPIS model in the interested area, hyper-parameters σ_f^2 and l associated to Eq. 13 are optimized first using the standard training method for Gaussian processes, i.e., maximizing the marginal likelihood. Then, we evaluate the local GP on voxel grid points at a resolution of 0.2 mm in the interested area and keep those points with zero mean of Eq. 14 as estimated points on the surface patch of the object.

Global Registration of Local Patches: With the calibrated object pose w.r.t. the gripper, we programmed the grasping system to follow a pre-defined path for object shape exploration. As is shown in Fig. 6B(iv), each time after GPIS query in the local 3D region, a global registration action is performed by transforming these local iso-surface points into the global space. Leveraging the continuous nature of the pre-defined exploration path, a simple surface registration strategy is used, where only the points of the estimated surface patch corresponding to moving distance are kept, and points of overlapping intervals belonging to the latest estimated surface patch are rejected. As is shown in Fig. 6C, after initialization of the relative pose between the gripper and the object, the shape of the object is continuously reconstructed using the described passive exploration strategy.

Object Shape Estimation Evaluation: In Fig. 6D, we present our method on real data collected during the underwater tactile exploration experiment. The shape estimates at each cutting sectional plane are compared concerning the ground truth using the Chamfer Distance (CD) [65], a commonly-used shape similarity metric. We chose five vertical

cutting planes and one horizontal sectional plane for reconstructed object surface evaluation. For each cutting plane, a calibration error exists between the vase and the Hand-E gripper, leading to the expected gap between the reconstructed and ground truth points. In addition to the systematic error, we have observed a slight decrease in the CD metric values between planes 1 and 5 compared to planes 2, 3, and 4, which could be attributed to the limitations of the soft finger in adapting to small objects with significant curvature. On the other hand, by employing tactile exploration actions with a relatively large contact area on the soft finger's surface, the shape estimation of objects similar in size to the vase can be accomplished more efficiently, typically within 8-12 touches. The 3D-printed vase has dimensions of approximately 80 mm by 80 mm by 140 mm.

6 Discussion

6.1 Sensorization of Soft Tactile Finger

Soft robots hold immense potential for delicate and controlled manipulation tasks, aiming to mimic the dexterity and adaptability of human hands [66]. Integrating high-resolution tactile sensing into such systems dramatically enhances their ability to perceive and understand the physical properties of objects they handle. However, equipping soft robots with comparable proprioceptive capabilities poses significant challenges, particularly for robotic fingers, which constantly interact with the environment and operate in confined spaces [67].

To overcome these challenges, researchers have explored various approaches. One strategy involves implementing soft and stretchable sensors that conform to the finger's shape [68], while another embeds sensors directly within the finger's structure. Vision-based tactile sensing presents a promising alternative, offering access to high-resolution contact information through an embedded camera [69]. Recent studies have successfully demonstrated the feasibility of this approach on rigid finger models [70], prompting exploration of its integration with compliant soft fingers [71, 72].

This study builds upon our previous work on soft finger design and in-finger camera integration to achieve underwater proprioceptive shape sensing. We developed a robust and cost-effective soft tactile finger design with transferable capabilities for underwater robotics applications by employing a simple waterproofing technique for the camera board.

6.2 Morphological Perception with Soft Robots

Morphological perception using soft bodies is a concept that involves utilizing the deformable nature of soft materials to enhance perception capabilities in robots [73]. Traditional rigid robots often struggle to adapt to complex environments and gather rich sensory information. Soft robots, on the other hand, leverage the deformability of soft materials to enhance their perception capabilities. These robots can actively change their shape and morphology by employing compliant materials or structures, interacting with the environment more nuancedly. This ability to deform in response to external stimuli becomes a powerful tool for perception [74]. It allows robots to "feel" their surroundings passively and gather information about object shape, texture, and internal composition [75].

Researchers have explored various soft robotic morphologies for object shape estimation. One approach utilizes curve-like tactile whiskers that bend and strain upon contact, providing information about the object's contour [76]. Another strategy employs flat elastomer pads that conform to the object's surface, estimating its shape through the pad's deformation [77]. Dome-shaped fingertips represent another morphology, using contact area and pressure distribution to infer shape and texture [78]. Each of these morphologies offers unique advantages and capabilities for accurate and versatile object shape estimation.

In this study, we propose a method that leverages the known deformation model of a specific soft finger to reconstruct its changing morphology during contact. The robot can make accurate proprioception state estimations using relatively sparse observations by understanding how the finger deforms based on its internal structure and material properties. This enhanced ability to perceive and interact with objects opens up exciting possibilities for robots operating in diverse and unpredictable environments.

7 Conclusion, Limitations, and Future Works

This paper presents a novel method for estimating a soft finger's deformation and contact surface using visual observations and a model-based approach. This "constrained geometry optimization" technique achieves efficient deformation reconstruction, comparable to traditional methods (e.g., ABAQUS) and modern alternatives (e.g., ARAP). Our method shows impressive speed, running nearly 40 times faster than ABAQUS while maintaining similar accuracy. Experimental validation demonstrates a median error of just 1.96 mm (2.1% of finger length) in overall body deformation estimation. Beyond deformation, we detail a promising pipeline for estimating the surface of contacted objects using

information about the finger's shape under pressure. This application is showcased underwater with soft tactile fingers integrated into a waterproof gripper.

However, certain limitations deserve consideration. Manufacturing inconsistencies inherent to soft robotics can impact the accuracy of our method. Algorithmic parameters also require precise calibration through physical experiments. Additionally, the rigid plate used for boundary condition acquisition slightly hampers the finger's compliance, affecting object-finger contact conformity. Finally, the object surface estimation pipeline is sensitive to contact geometry, restricting its use to local surface patches with smooth curvature changes.

Future research seeks to optimize the system for versatile tactile grasping and expand its integration into robotic grippers for diverse land and underwater applications. Furthermore, the vision-based proprioception method holds the potential for developing advanced robotic necks with precise state estimation in amphibious robots driven by parallel mechanisms or pneumatic actuation.

Acknowledgments

Appendix

- **Movie S1. Evaluation of State Estimation with Motion Capture System.** In this movie, we demonstrate four different contact configurations tested using the test platform and present the error measurement protocol utilized in Experiment Section 5.2.
- **Movie S2. Estimating State when Deformed by Touch Haptic Device.** In this movie, we showcase the experimental procedures described in Experiment Section 5.3. These involve measuring the position discrepancy between the pen-nib and the nearest node on the soft finger, representing the estimated deformation field error sampled at the corresponding location.
- **Movie S3. Shape Sensing of a Vase Underwater.** This movie features a demonstration of the experiment setup described in Experiment Section 5.4. It provides a comprehensive overview of the entire experimental process and showcases the results obtained from estimating the shape of an underwater vase using the soft finger.

References

[1] Ravinder S Dahiya, Giorgio Metta, Maurizio Valle, and Giulio Sandini. Tactile sensing—from humans to humanoids. *IEEE Transactions on Robotics*, 26(1):1–20, 2009.

[2] Roland S Johansson and J Randall Flanagan. Coding and use of tactile signals from the fingertips in object manipulation tasks. *Nature Reviews Neuroscience*, 10(5):345–359, 2009.

[3] Subramanian Sundaram, Petr Kellnhofer, Yunzhu Li, Jun-Yan Zhu, Antonio Torralba, and Wojciech Matusik. Learning the signatures of the human grasp using a scalable tactile glove. *Nature*, 569(7758):698–702, 2019.

[4] Sungwoo Chun, Jong-Seok Kim, Yongsang Yoo, Youngin Choi, Sung Jun Jung, Dongpyo Jang, Gwangyeob Lee, Kang-Il Song, Kum Seok Nam, Inchan Youn, et al. An artificial neural tactile sensing system. *Nature Electronics*, 4(6):429–438, 2021.

[5] Ravinder S. Dahiya, Philipp Mittendorfer, Maurizio Valle, Gordon Cheng, and Vladimir J. Lumelsky. Directions toward effective utilization of tactile skin: A review. *IEEE Sensors Journal*, 13(11):4121–4138, 2013.

[6] Benjamin Shih, Dylan Shah, Jinxing Li, Thomas G Thuruthel, Yong-Lae Park, Fumiya Iida, Zhenan Bao, Rebecca Kramer-Bottiglio, and Michael T Tolley. Electronic skins and machine learning for intelligent soft robots. *Science Robotics*, 5(41):eaaz9239, 2020.

[7] OpenAI: Marcin Andrychowicz, Bowen Baker, Maciek Chociej, Rafal Jozefowicz, Bob McGrew, Jakub Pachocki, Arthur Petron, Matthias Plappert, Glenn Powell, Alex Ray, et al. Learning dexterous in-hand manipulation. *The International Journal of Robotics Research*, 39(1):3–20, 2020.

[8] Zhanat Kappassov, Juan-Antonio Corrales, and Véronique Perdereau. Tactile sensing in dexterous robot hands. *Robotics and Autonomous Systems*, 74:195–220, 2015.

[9] Hanna Yousef, Mehdi Boukallel, and Kaspar Althoefer. Tactile sensing for dexterous in-hand manipulation in robotics—a review. *Sensors and Actuators A: physical*, 167(2):171–187, 2011.

[10] Qiang Li, Oliver Kroemer, Zhe Su, Filipe Fernandes Veiga, Mohsen Kaboli, and Helge Joachim Ritter. A review of tactile information: Perception and action through touch. *IEEE Transactions on Robotics*, 36(6):1619–1634, 2020.

[11] Giuseppe De Maria, Ciro Natale, and Salvatore Pirozzi. Force/tactile sensor for robotic applications. *Sensors and Actuators A: Physical*, 175:60–72, 2012.

[12] Emanuele Magrini, Fabrizio Flacco, and Alessandro De Luca. Estimation of contact forces using a virtual force sensor. In *IEEE International Conference on Intelligent Robots and Systems*, pages 2126–2133. IEEE, 2014.

[13] Rachel Holladay, Tomás Lozano-Pérez, and Alberto Rodriguez. Planning for multi-stage forceful manipulation. In *IEEE International Conference on Robotics and Automation*, pages 6556–6562. IEEE, 2021.

[14] Hsiu-Chin Lin and Michael Mistry. Contact surface estimation via haptic perception. In *IEEE International Conference on Robotics and Automation*, pages 5087–5093. IEEE, 2020.

[15] Sami Haddadin, Lars Johannsmeier, and Fernando Díaz Ledezma. Tactile robots as a central embodiment of the tactile internet. *Proceedings of the IEEE*, 107(2):471–487, 2018.

[16] Yuanzhao Wu, Yiwei Liu, Youlin Zhou, Qikui Man, Chao Hu, Waqas Asghar, Fali Li, Zhe Yu, Jie Shang, Gang Liu, et al. A skin-inspired tactile sensor for smart prosthetics. *Science Robotics*, 3(22):eaat0429, 2018.

[17] Fengyuan Liu, Sweety Deswal, Adamos Christou, Mahdieh Shojaei Baghini, Radu Chirila, Dhayalan Shakthivel, Moupali Chakraborty, and Ravinder Dahiya. Printed synaptic transistor–based electronic skin for robots to feel and learn. *Science Robotics*, 7(67):eabl7286, 2022.

[18] Youcan Yan, Zhe Hu, Zhengbao Yang, Wenzhen Yuan, Chaoyang Song, Jia Pan, and Yajing Shen. Soft magnetic skin for super-resolution tactile sensing with force self-decoupling. *Science Robotics*, 6(51):eabc8801, 2021.

[19] Wenzhen Yuan, Siyuan Dong, and Edward H Adelson. Gelsight: High-resolution robot tactile sensors for estimating geometry and force. *Sensors*, 17(12):2762, 2017.

[20] Benjamin Ward-Cherrier, Nicholas Pestell, Luke Cramphorn, Benjamin Winstone, Maria Elena Giannaccini, Jonathan Rossiter, and Nathan F Lepora. The tactip family: Soft optical tactile sensors with 3d-printed biomimetic morphologies. *Soft Robotics*, 5(2):216–227, 2018.

[21] Alex Alspach, Kunimatsu Hashimoto, Naveen Kuppuswamy, and Russ Tedrake. Soft-bubble: A highly compliant dense geometry tactile sensor for robot manipulation. In *IEEE International Conference on Soft Robotics*, pages 597–604. IEEE, 2019.

[22] Huanbo Sun and Georg Martius. Guiding the design of superresolution tactile skins with taxel value isolines theory. *Science Robotics*, 7(63):eabm0608, 2022.

[23] Camill Trueeb, Carmelo Sferrazza, and Raffaello D'Andrea. Towards vision-based robotic skins: a data-driven, multi-camera tactile sensor. In *2020 IEEE International Conference on Soft Robotics*, pages 333–338. IEEE, 2020.

[24] Carmelo Sferrazza, Adam Wahlsten, Camill Trueeb, and Raffaello D'Andrea. Ground truth force distribution for learning-based tactile sensing: A finite element approach. *IEEE Access*, 7:173438–173449, 2019.

[25] Akihiko Yamaguchi and Christopher G Atkeson. Recent progress in tactile sensing and sensors for robotic manipulation: can we turn tactile sensing into vision? *Advanced Robotics*, 33(14):661–673, 2019.

[26] Costanza Armanini, Frédéric Boyer, Anup Teejo Mathew, Christian Duriez, and Federico Renda. Soft robots modeling: A structured overview. *IEEE Transactions on Robotics*, 2023.

[27] Akihiko Yamaguchi and Christopher G Atkeson. Implementing tactile behaviors using fingervision. In *IEEE-RAS International Conference on Humanoid Robotics*, pages 241–248. IEEE, 2017.

[28] Till Kroeger, Radu Timofte, Dengxin Dai, and Luc Van Gool. Fast optical flow using dense inverse search. In *European Conference on Computer Vision*, pages 471–488. Springer, 2016.

[29] Carmelo Sferrazza and Raffaello D'Andrea. Design, motivation and evaluation of a full-resolution optical tactile sensor. *Sensors*, 19(4):928, 2019.

[30] Zhongkai Zhang, Jérémie Dequidt, and Christian Duriez. Vision-based sensing of external forces acting on soft robots using finite element method. *IEEE Robotics and Automation Letters*, 3(3):1529–1536, 2018.

[31] Qiang Li, Oliver Kroemer, Zhe Su, Filipe Fernandes Veiga, Mohsen Kaboli, and Helge Joachim Ritter. A review of tactile information: Perception and action through touch. *IEEE Transactions on Robotics*, 36(6):1619–1634, 2020.

[32] Mohsen Kaboli, Kunpeng Yao, Di Feng, and Gordon Cheng. Tactile-based active object discrimination and target object search in an unknown workspace. *Autonomous Robots*, 43:123–152, 2019.

[33] Jarmo Ilonen, Jeannette Bohg, and Ville Kyrki. Three-dimensional object reconstruction of symmetric objects by fusing visual and tactile sensing. *The International Journal of Robotics Research*, 33(2):321–341, 2014.

[34] Shaoxiong Wang, Jiajun Wu, Xingyuan Sun, Wenzhen Yuan, William T Freeman, Joshua B Tenenbaum, and Edward H Adelson. 3d shape perception from monocular vision, touch, and shape priors. In *IEEE International Conference on Intelligent Robots and Systems*, pages 1606–1613. IEEE, 2018.

[35] Oncay Yasa, Yasunori Toshimitsu, Mike Y Michelis, Lewis S Jones, Miriam Filippi, Thomas Buchner, and Robert K Katzschmann. An overview of soft robotics. *Annual Review of Control, Robotics, and Autonomous Systems*, 6:1–29, 2023.

[36] Mohammed Rafeeq, Siti Fauziah Toha, Salmiah Ahmad, and Mohd Asyraf Razib. Locomotion strategies for amphibious robots-a review. *IEEE Access*, 9:26323–26342, 2021.

[37] Junzhi Yu, Rui Ding, Qinghai Yang, Min Tan, Weibing Wang, and Jianwei Zhang. On a bio-inspired amphibious robot capable of multimodal motion. *IEEE/ASME Transactions on Mechatronics*, 17(5):847–856, 2012.

[38] Rafsan Al Shafatul Islam Subad, Liam B. Cross, and Kihan Park. Soft robotic hands and tactile sensors for underwater robotics. *Applied Mechanics*, 2(2):356–382, 2021.

[39] Lei Li, Wenbo Liu, Bocheng Tian, Peiyu Hu, Wenzhuo Gao, Yuchen Liu, Fuqiang Yang, Youning Duo, Hongru Cai, Yiyuan Zhang, et al. An aerial–aquatic hitchhiking robot with remora-inspired tactile sensors and thrust vectoring units. *Advanced Intelligent Systems*, page 2300381, 2023.

[40] Achint Aggarwal, Peter Kampmann, Johannes Lemburg, and Frank Kirchner. Haptic object recognition in underwater and deep-sea environments. *Journal of field robotics*, 32(1):167–185, 2015.

[41] Shangkui Yang, Yongxiang Zhou, Ian D. Walker, Chenghao Yang, David T. Branson, Zhibin Song, Jian Sheng Dai, and Rongjie Kang. Dynamic capture using a traplike soft gripper with stiffness anisotropy. *IEEE/ASME Transactions on Mechatronics*, 28(3):1337–1346, 2023.

[42] Zeyi Yang, Sheng Ge, Fang Wan, Yujia Liu, and Chaoyang Song. Scalable tactile sensing for an omni-adaptive soft robot finger. In *IEEE International Conference on Soft Robotics*, pages 572–577, 2020.

[43] Linhan Yang, Fang Wan, Haokun Wang, Xiaobo Liu, Yujia Liu, Jia Pan, and Chaoyang Song. Rigid-soft interactive learning for robust grasping. *IEEE Robotics and Automation Letters*, 5(2):1720–1727, 2020.

[44] Fang Wan, Xiaobo Liu, Ning Guo, Xudong Han, Feng Tian, and Chaoyang Song. Visual learning towards soft robot force control using a 3d metamaterial with differential stiffness. In *Conference on Robot Learning*, pages 1269–1278. PMLR, 2022.

[45] Fang Wan, Haokun Wang, Jiyuan Wu, Yujia Liu, Sheng Ge, and Chaoyang Song. A reconfigurable design for omni-adaptive grasp learning. *IEEE Robotics and Automation Letters*, 5(3):4210–4217, 2020.

[46] Cornelius Lanczos. *The variational principles of mechanics*. Courier Corporation, 2012.

[47] Andreas Longva, Fabian Löschner, Tassilo Kugelstadt, José Antonio Fernández-Fernández, and Jan Bender. Higher-order finite elements for embedded simulation. *ACM Transactions on Graphics*, 39(6), nov 2020.

[48] Noam Aigerman and Yaron Lipman. Injective and bounded distortion mappings in 3d. *ACM Transactions on Graphics*, 32(4):1–14, 2013.

[49] Ligang Liu, Lei Zhang, Yin Xu, Craig Gotsman, and Steven J Gortler. A local/global approach to mesh parameterization. In *Computer Graphics Forum*, volume 27, pages 1495–1504. Wiley, 2008.

[50] Noam Aigerman, Roi Poranne, and Yaron Lipman. Seamless surface mappings. *ACM Transactions on Graphics*, 34(4), jul 2015.

[51] Jason Smith and Scott Schaefer. Bijective parameterization with free boundaries. *ACM Transactions on Graphics*, 34(4):1–9, 2015.

[52] W Michael Lai, David Rubin, and Erhard Krempl. *Introduction to Continuum Mechanics*. Butterworth-Heinemann, 2009.

[53] Michael Rabinovich, Roi Poranne, Daniele Panozzo, and Olga Sorkine-Hornung. Scalable locally injective mappings. *ACM Transactions on Graphics*, 36(2), apr 2017.

[54] Edith Tretschk, Navami Kairanda, Mallikarjun BR, Rishabh Dabral, Adam Kortylewski, Bernhard Egger, Marc Habermann, Pascal Fua, Christian Theobalt, and Vladislav Golyanik. State of the art in dense monocular non-rigid 3d reconstruction. In *Computer Graphics Forum*, volume 42, pages 485–520. Wiley Online Library, 2023.

[55] Marcos P Gerardo-Castro, Thierry Peynot, and Fabio Ramos. Laser-radar data fusion with gaussian process implicit surfaces. In *International Conference on Field and Service Robotics*, pages 289–302. Springer, 2015.

[56] Oliver Williams and Andrew Fitzgibbon. Gaussian process implicit surfaces. In *Gaussian Processes in Practice*, 2006.

[57] Stanimir Dragiev, Marc Toussaint, and Michael Gienger. Gaussian process implicit surfaces for shape estimation and grasping. In *IEEE International Conference on Robotics and Automation*, pages 2845–2850. IEEE, 2011.

[58] Simon Ottenhaus, Martin Miller, David Schiebener, Nikolaus Vahrenkamp, and Tamim Asfour. Local implicit surface estimation for haptic exploration. In *IEEE International Conference on Humanoid Robots*, pages 850–856. IEEE, 2016.

[59] Carl Edward Rasmussen and Christopher K. I. Williams. *Gaussian Processes for Machine Learning*. The MIT Press, 11 2005.

[60] Patrick Peltzer, Johannes Lotz, and Uwe Naumann. Eigen-ad: Algorithmic differentiation of the eigen library. In *International Conference on Computational Science*, page 690–704, Berlin, Heidelberg, 2020. Springer-Verlag.

[61] Guoxin Fang, Christopher-Denny Matte, Rob BN Scharff, Tsz-Ho Kwok, and Charlie CL Wang. Kinematics of soft robots by geometric computing. *IEEE Transactions on Robotics*, 36(4):1272–1286, 2020.

[62] Sergio Garrido-Jurado, Rafael Muñoz-Salinas, Francisco José Madrid-Cuevas, and Manuel Jesús Marín-Jiménez. Automatic generation and detection of highly reliable fiducial markers under occlusion. *Pattern Recognition*, 47(6):2280–2292, 2014.

[63] Thomas Martin Lehmann, Claudia Gonner, and Klaus Spitzer. Survey: Interpolation methods in medical image processing. *IEEE Transactions on Medical Imaging*, 18(11):1049–1075, 1999.

[64] Ning Guo, Xudong Han, Xiaobo Liu, Shuqiao Zhong, Zhiyuan Zhou, Jian Lin, Jiansheng Dai, Fang Wan, and Chaoyang Song. Autoencoding a soft touch to learn grasping from on-land to underwater. *Advanced Intelligent Systems*, page 2300382, 2023.

[65] A. Thayananthan, B. Stenger, P.H.S. Torr, and R. Cipolla. Shape context and chamfer matching in cluttered scenes. In *IEEE Computer Society Conference on Computer Vision and Pattern Recognition*, volume 1, pages I–I, 2003.

[66] Steffen Puhlmann, Jason Harris, and Oliver Brock. Rbo hand 3: A platform for soft dexterous manipulation. *IEEE Transactions on Robotics*, 38(6):3434–3449, 2022.

[67] Abdul Ghafoor, Jian S Dai, and Joseph Duffy. Stiffness modeling of the soft-finger contact in robotic grasping. *Journal of Mechanical Design*, 126(4):646–656, 2004.

[68] Sihong Wang, Jie Xu, Weichen Wang, Ging-Ji Nathan Wang, Reza Rastak, Francisco Molina-Lopez, Jong Won Chung, Simiao Niu, Vivian R Feig, Jeffery Lopez, et al. Skin electronics from scalable fabrication of an intrinsically stretchable transistor array. *Nature*, 555(7694):83–88, 2018.

[69] Javier Tapia, Espen Knoop, Mojmir Mutnỳ, Miguel A Otaduy, and Moritz Bächer. Makesense: Automated sensor design for proprioceptive soft robots. *Soft Robotics*, 7(3):332–345, 2020.

[70] Huanbo Sun, Katherine J Kuchenbecker, and Georg Martius. A soft thumb-sized vision-based sensor with accurate all-round force perception. *Nature Machine Intelligence*, 4(2):135–145, 2022.

[71] Sandra Q. Liu and Edward H. Adelson. Gelsight fin ray: Incorporating tactile sensing into a soft compliant robotic gripper. In *IEEE International Conference on Soft Robotics*, pages 925–931, 2022.

[72] Sandra Q. Liu, Yuxiang Ma, and Edward H. Adelson. Gelsight baby fin ray: A compact, compliant, flexible finger with high-resolution tactile sensing. In *IEEE International Conference on Soft Robotics*, pages 1–8, 2023.

[73] Nhan Huu Nguyen and Van Anh Ho. Mechanics and morphological compensation strategy for trimmed soft whisker sensor. *Soft Robotics*, 9(1):135–153, 2022.

[74] Hongbo Wang, Massimo Totaro, and Lucia Beccai. Toward perceptive soft robots: Progress and challenges. *Advanced Science*, 5(9):1800541, 2018.

[75] Omar Faris, Rajkumar Muthusamy, Federico Renda, Irfan Hussain, Dongming Gan, Lakmal Seneviratne, and Yahya Zweiri. Proprioception and exteroception of a soft robotic finger using neuromorphic vision-based sensing. *Soft Robotics*, 10(3):467–481, 2023. PMID: 36251962.

[76] Chenxi Xiao, Shujia Xu, Wenzhuo Wu, and Juan Wachs. Active multiobject exploration and recognition via tactile whiskers. *IEEE Transactions on Robotics*, 38(6):3479–3497, 2022.

[77] Martin Meier, Matthias Schopfer, Robert Haschke, and Helge Ritter. A probabilistic approach to tactile shape reconstruction. *IEEE Transactions on Robotics*, 27(3):630–635, 2011.

[78] Nathan F Lepora and John Lloyd. Optimal deep learning for robot touch: Training accurate pose models of 3d surfaces and edges. *IEEE Robotics & Automation Magazine*, 27(2):66–77, 2020.